

GT2016-57241

NUMERICAL INVESTIGATION OF THREE-DIMENSIONAL SEPARATION IN AN AXIAL FLOW COMPRESSOR: THE INFLUENCE OF FREE-STREAM TURBULENCE INTENSITY AND ENDWALL BOUNDARY LAYER STATE

Ashley D. Scillitoe^{1*}, Paul G. Tucker¹, Paolo Adami²

¹CFD Laboratory, Department of Engineering, University of Cambridge, Cambridge,
CB2 1PZ, UK

²Core CFD Team Leader, CFD Methods, Rolls-Royce Deutschland, Eschenweg 11,
15827 Blankenfelde-Mahlow, Germany

ABSTRACT

Regions of three-dimensional separations are an inherent flow feature of the suction surface - endwall corner in axial compressors. These corner separations can cause a significant total pressure loss and reduce the compressor's efficiency. This paper uses wall-resolved LES to investigate the loss sources in a corner separation, and examines the influence of the inflow turbulence on these sources.

Different subgrid scale (SGS) models are tested and the choice of model is found to be important. The σ SGS model, which performed well, is then used to perform LES of a compressor endwall flow. The time-averaged data is in good agreement with measurements. The viscous and turbulent dissipation are used to highlight the sources of loss, with the latter being dominant. The key loss sources are seen to be the 2D laminar separation bubble and trailing edge wake, and the 3D flow region near the endwall.

Increasing the free-stream turbulence intensity (FST) changes the suction surface boundary layer transition mode from separation induced to bypass. However, it doesn't significantly alter the transition location and therefore the corner separation size. Additionally, the FST doesn't noticeably interact with the corner separation itself, meaning that in this case the corner separation is relatively insensitive to the FST.

The endwall boundary layer state is found to be significant. A laminar endwall boundary layer separates much earlier leading to a larger passage vortex. This significantly alters the endwall flow and loss. Hence, the need for accurate boundary measurements is clear.

INTRODUCTION

Over-turning of the endwall boundary layer causes a three-dimensional separation to form in the corner formed by the suction surface and endwall of axial compressors. A number of studies have discussed the importance of these corner separations in both stator and rotor blades [1, 2]. They can cause passage blockage and effectively limit the loading and static pressure rise achievable by the compressor. Additionally, they may cause a significant total pressure and a reduction in the compressor's efficiency.

Traditionally, the size of three-dimensional separations has been correlated to global parameters such as inlet and exit flow angles, and pitch to chord ratio. An example of this is the endwall diffusion parameter and corner stall metric proposed by Lei et al. [3]. These are useful in the early design stage, but to maximise the compressor efficiency it is important to consider the 3D separation in more detail. For example: Goodhand and Miller [4] examine the sensitivity of the 3D separation to small leading edge geometry features, while Gbadebo et al. [5] study the influence of surface roughness on the 3D separation. Both of these studies conclude that any process leading to premature boundary layer transition on the early suction surface, near the endwalls, will dramatically increase the size of the 3D separation. This is due to the suction surface boundary layer being excessively thickened.

Premature suction surface boundary layer transition may be caused by leading edge geometry or surface roughness, however it could also be caused by incoming free-stream turbulence (FST). Zaki et al. [6] use direct numerical simulation (DNS) to study the influence of FST intensity on the transitional processes on a compressor blade. They find that the mode and location of the boundary layer

*Address all correspondence to this author (as2341@cam.ac.uk).

transition is very sensitive to the FST intensity. This was at a Reynolds number of $Re_c = 0.14 \times 10^6$, and this sensitivity would be expected to decrease at higher Reynolds numbers, with the boundary layers eventually becoming fully turbulent. However, Steinert and Starken [7] showed experimentally that at $Re_c = 0.84 \times 10^6$ and $T_i = 2.5\%$ the suction surface boundary layer stayed laminar to peak suction over a wide range of incidences. At cruise, Reynolds numbers between 0.4×10^6 and 1.6×10^6 are seen in aero-gas turbine compressors [4]. Therefore the FST may have an important effect on the 3D corner separation in compressors.

With the above in mind, this paper presents a series of numerical investigations intended to address the following:

- The effect of the FST intensity on the suction surface boundary layer, and therefore the 3D corner separation, is examined. The existence of any direct interactions between the FST and corner separation is also considered.
- Gbadebo [8] found that the 3D separation is also sensitive to the thickness of the incoming endwall boundary layer. Taking this further this paper examines whether the endwall boundary layer state (i.e. laminar vs turbulent) is important.
- Denton [9] investigated the loss sources in the 3D separation region using the entropy generation rate. In a similar manner this paper uses the viscous and turbulent dissipation to identify the loss sources. In particular the effect of the inflow conditions on these loss sources will be studied.

Large eddy simulation (LES) will be used for the numerical investigations outlined above. Lardeau et al. [10] found that LES can successfully predict the transitional processes occurring in a compressor flow, at a fraction of the cost of a DNS. However, the sub-grid scale (SGS) models used (MTS and dynamic Smagorinsky) require additional filtering which is problematic for the 3D endwall geometry considered here. To investigate whether such advanced SGS models are necessary a number of purely local SGS models are first tested on a simpler quasi-2D blade geometry.

FLOW CONFIGURATIONS

The two linear compressor blade cascades detailed in Tab. 1 are simulated in this paper. Both are representative of highly loaded compressor stator blades found in a modern gas-turbine compressor. Cascade 1 consists of NACA-65 aerofoils and was tested experimentally by Hilgenfeld and Pfitzner [11]. This cascade was also simulated at a lower Re_c using DNS by Zaki et al. [6] and using LES by Lardeau et al. [10]. Cascade 2 is a linear CDA (Controlled Diffusion Aerofoil) cascade investigated experimentally by Gbadebo et al. [8, 12].

The computational grid for cascade 2 is displayed in Fig. 1. A similar H-O-H topology is used for cascade 1. Downstream of the blade a sponge zone is used to prevent reflections from the outflow boundary. Pitchwise periodicity is enforced with periodic boundaries at mid-pitch. Some of the cases run are spanwise periodic (i.e. no

TABLE 1: GEOMETRICAL AND INFLOW PARAMETERS FOR THE TWO COMPRESSOR CASCADES.

	Cascade 1	Cascade 2
Blade profile	NACA-65	CDA
Re_c	1.38×10^5 (DNS)	2.30×10^5
h/c	1.36	1.32
S/c	0.55	0.926
t/c	0.055	0.1
i ($^\circ$)	-6.0	0.0
Flow turning ($^\circ$)	36.0	33.0
2D Diffusion Factor	0.42	0.49

endwalls), with periodic boundaries in the spanwise direction. The spanwise extent of these cases is set to 20% span to match the Zaki et al. DNS case [6]. The cascade 2 geometry is symmetric about the mid-span, however to prevent contamination of the flow near the mid-span, an inviscid wall is placed at 65% span for the cases with an endwall. The endwall is represented by a no-slip wall.

The O-mesh for cascade 1 has dimensions $690 \times 45 \times 136$ and for cascade 2 it has dimensions $726 \times 60 \times 557$. Approximately 9.3M grid points are used in the cascade 1 mesh and 69M for cascade 2. The mesh for cascade 2 is significantly larger due to the larger span, higher Re_c , and need to resolve the endwall boundary layer. For all the cases $\Delta^+ < 50/1/15$ in the wall tangential/normal/spanwise directions at the wall. These grid resolutions are well within the recommended values for wall-resolved LES given by Piomelli and Chasnov [13].

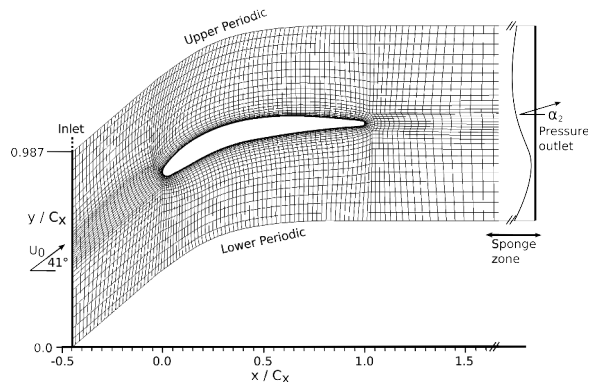


FIGURE 1: 2D SLICE OF COMPUTATIONAL GRID FOR CASCADE 2, SHOWING EVERY 5TH GRID POINT.

The LES cases run for this paper are listed in Tab. 2. Case 1-L-N is a quasi-2D case, with spanwise periodic boundaries. The

TABLE 2: CASES SIMULATED.

Case	Cascade	Endwall present?	FST Intensity, T_i	Endwall BL
1-L-N	1	No	Low (3.25%)	N/A
2-L-N	2	No	Low (1.0%)	N/A
2-L-LBL	2	Yes	Low (1.0%)	LBL
2-L-TBL	2	Yes	Low (1.0%)	TBL
2-H-TBL	2	Yes	High (10.0%)	TBL

inflow turbulence intensity (T_i) is set at 3.25% to match the DNS of Zaki et al. [6]. This case is used to investigate the performance of a number of sub-grid scale models in a transitional compressor flow.

To investigate the effect of inflow conditions on the endwall flow region three simulations of cascade 2 are run with different inflow conditions. Case 2-L-TBL is intended to match the experiment run by Gbadebo et al. [8, 12]. The endwall boundary layer and the FST intensity are measured in the experiment $2C$ upstream of the leading edge. To determine the boundary layer parameters at the LES inflow location the boundary layer from a precursor RANS simulation is measured at $x/C_x = -0.45$, and the results are presented in Table 3.

TABLE 3: ENDWALL BOUNDARY LAYER PARAMETERS.

$x =$	$-2.0C$	$-0.45C_x$
δ_0	$0.036C_x$	$0.060C_x$
Re_θ	440	1350
Re_{δ^*}	770	1850
H	1.75	1.37

The measured shape factor and velocity profile at $x = -2C$ suggests the boundary layer is neither fully laminar nor turbulent, with it perhaps having been partly relaminarised by the upstream contraction in the test rig. Hence there is a degree of uncertainty here since the RANS simulation assumes a fully turbulent boundary layer at $x/C = -2$.

The inflow FST intensity in the cascade 2 experiment is 1.5% [8]. To estimate the FST intensity at the LES inflow ($x/C_x = -0.45$) the following equation from Spalart and Rumsey [14] is used:

$$k = k_{FS} \left[1 + (C_{\epsilon 2} - 1) \left(\frac{\epsilon}{k} \right)_{FS} \frac{x}{U_1} \right]^{\frac{-1}{C_{\epsilon 2} - 1}} \quad (1)$$

where FS denotes the original inflow conditions at $x/C = -0.2$ and k is the free-stream turbulent kinetic energy at $x/C_x = -0.45$.

Approximating $\epsilon_{FS} = k_{FS}^{3/2}/L_\epsilon$, with $L_\epsilon = 2.2L$, gives an FST intensity $T_i \approx 1.0\%$ at $x/C_x = -0.45$. The integral length scale of the free-stream turbulence is chosen as $L = 0.06C_x$ for all cases, which is the same as that used in the simulations of Zaki et al [6].

NUMERICAL METHOD

The code used is the Rolls-Royce CFD code *Hydra* [15]. It is a second-order unstructured, mixed element, compressible finite-volume code. Temporal discretisation is performed with a standard five-stage Runge-Kutta algorithm. To improve the code's performance at low Mach numbers, the code has been modified to evaluate the pressure using an artificial compressibility method [16]. This modified code has been successfully used for a number of low pressure turbine LES studies [17, 18].

Sub-Grid Scale Modelling

In order to examine the effect of sub-grid scale (SGS) modelling on transitional compressor flows a number of SGS models are investigated in this paper.

The first SGS model used is the Smagorinsky model [19] which defines the SGS viscosity as:

$$\mu_{sgs} = \rho \Delta_{sgs}^2 \sqrt{2S_{ij}S_{ij}} \quad (2)$$

where S_{ij} is the instantaneous strain rate tensor. The Smagorinsky model is still one of the most widely used SGS models, despite it having some major limitations [20]. For example: incorrect limiting behaviour near the wall and the model not vanishing in laminar flow. The model's near-wall behaviour is improved here by using wall damping $\Delta_{sgs} = \min(C_s \Delta_{vol}, \kappa d)$, however this still gives $\mu_{sgs} = O(d^2)$ instead of the desired $\mu_{sgs} = O(d^3)$.

One way to solve the above problems is to modify the Smagorinsky constant C_s dynamically, as is done in the procedure proposed by Germano et al. [20]. However, this requires additional filtering making it expensive and impractical for LES of complex geometries. As an alternative Nicoud and Ducros [21] propose the Wall-Adapting-Local-Eddy-viscosity (WALE) model:

$$\mu_{sgs} = \rho (C_w \Delta_{vol})^2 \frac{(S_{ij}^d S_{ij}^d)^{3/2}}{(S_{ij} S_{ij})^{5/2} + (S_{ij}^d S_{ij}^d)^{5/4}} \quad (3)$$

The $S_{ij}^d S_{ij}^d$ term is based on both strain and vorticity and is formulated to give zero SGS viscosity in pure shear regions such as a laminar boundary layer.

The final model tested is the σ model also proposed by Nicoud et al. [22], which bases the SGS viscosity on the singular values ($\sigma_1, \sigma_2, \sigma_3$) of the resolved velocity gradient tensor:

$$\mu_{sgs} = \rho (C_\sigma \Delta_{vol})^2 \frac{\sigma_3 (\sigma_1 - \sigma_2)(\sigma_2 - \sigma_3)}{\sigma_1} \quad (4)$$

In addition to correctly returning zero SGS viscosity in the case of pure shear, the σ model also correctly gives zero SGS viscosity for solid rotation, plus axisymmetric and isotropic contraction/expansion. Both the WALE and σ models also give $\mu_{sgs} = O(d^3)$ as desired.

The WALE and σ model constants recommended by Nicoud et al. [21, 22] ($C_w = 0.5$ and $C_\sigma = 1.35$) are used. For isotropic decaying turbulence these constants give dissipation equal to using the Smagorinsky model with $C_s \approx 0.165$, therefore this value is chosen for the Smagorinsky model here.

Time Dependent Inflow Conditions

For the endwall test case with an incoming laminar boundary layer (Case 2-L-LBL) an approximate sinusoidal blasius velocity profile is prescribed with $\delta_0 = 0.06C_x$. For the cases with a turbulent endwall boundary layer (TBL) at the inflow (2-L-TBL and 2-H-TBL) a precursor LES was performed to obtain the time-series data of the incoming TBL. Lund's recycling/rescaling technique [23] is used to generate a streamwise growing TBL, and the time-series data is saved at $Re_\theta = 1350$. The generated LBL and TBL are seen to have the same δ_0 thickness in Fig. 2a. The velocity fluctuations and shear stress profiles for the generated TBL also agree well with a DNS of a TBL ($Re_\theta = 1410$) performed by Spalart [24], as shown in Fig. 2b.

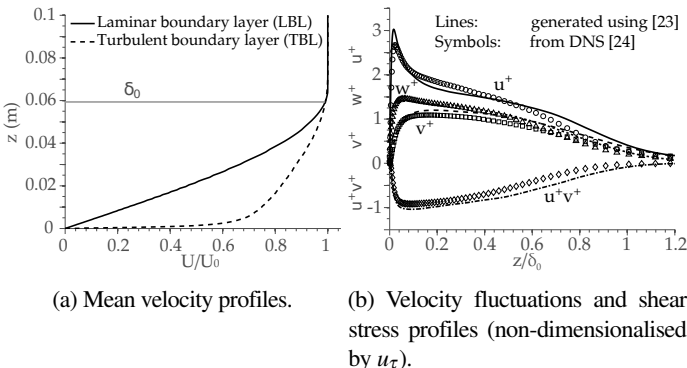


FIGURE 2: ENDWALL BOUNDARY LAYER PROFILES AT INFLOW.

For all the test cases free-stream velocity fluctuations were superimposed onto the mean inflow velocity. These quasi-isotropic perturbations were synthetically generated by a code kindly provided by Dr. Lardeau. The code uses a Fourier-series method [21], and the fluctuations generated satisfy both continuity and the modified von Karman energy spectrum, given by:

$$E(\kappa) = \frac{2}{3} \frac{a(\kappa/\kappa_p)^4}{(b + (\kappa/\kappa_p)^2)^{17/6}} \quad (5)$$

where $a = 1.606$, $b = 1.35$, κ is the wave number, and κ_p is the wave

number of maximum energy ($\kappa_p = 1.8/L$). For further details see Refs. [10, 25].

Simulation Time/Cost

The time-step is set to give $CFL_{max} \approx 0.8$, and a flow-through time (T^*) equates to approximately 10000 time-steps. The simulations were run for $4T^*$ to clear the initial transients. The quasi-2D cases were then run for $4T^*$ to collect statistics, while the fully 3D cases had to be run for $10T^*$ due to the lack of spanwise averaging.

All simulations were run on ARCHER, the UK's National HPC facility. ARCHER is a Cray XC30 MPP supercomputer consisting of 4920 compute nodes, each with two 12-core Intel Ivy Bridge Processors. The quasi-2D cases were run on 128 cores, with each case requiring 12k CPU hours in total. The fully 3D cases were run on 960 cores, with each case requiring 161k CPU hours in total.

CASCADE 1: QUASI-2D CASE

In this section the LES case 1-L-N is compared to DNS case T1 of Zaki et al. [6]. Figure 3 gives a visual representation of the boundary layer transition processes on the blade surfaces. The Q-criterion, which represents the local balance between shear strain and vorticity magnitude, is used to identify vortices. Qualitatively the LES agrees well with the DNS:

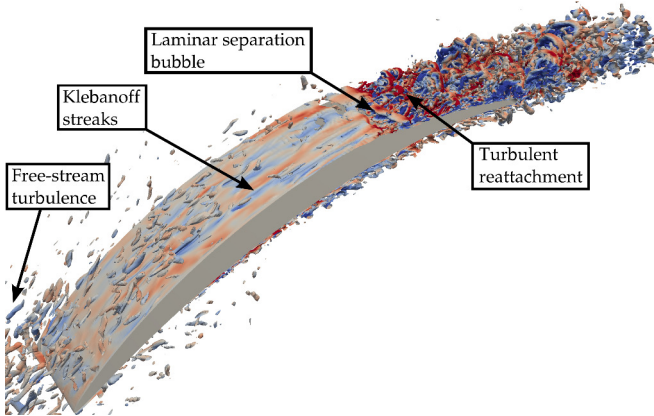
Figure 3a: Suction surface A region of elongated low and high speed streaks is observed upstream of transition. The attached laminar boundary layer then separates. In this laminar separation region, or "bubble", spanwise orientated structures associated with Kelvin-Helmholtz (KH) modes are seen. Transition occurs here, and the flow then reattaches to form a turbulent boundary layer.

Figure 3b: Pressure surface Transition to turbulence occurs much earlier here. A "natural" transition involving the amplification of Tollmien-Schlichting (TS) waves is bypassed due to the FST. However, Λ structures were observed in the DNS. These are often an indication of natural transition mechanisms [6], implying that the FST intensity may not be high enough for natural transition to be completely bypassed. Such structures are also observed in the LES as shown in Fig. 3b.

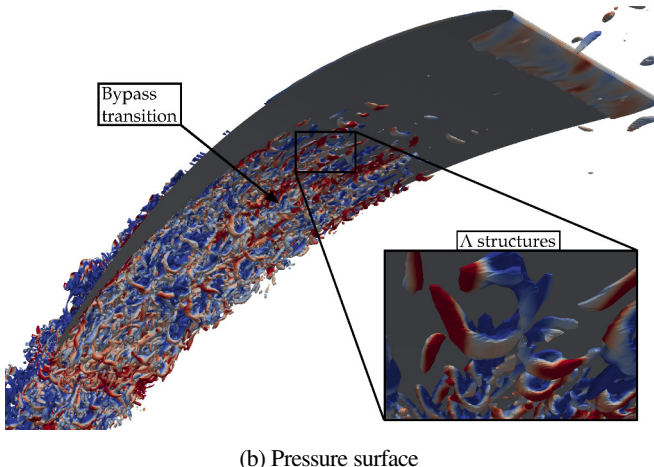
The flow on both surfaces is now analysed in more detail, with particular emphasis on the sensitivity to the SGS model.

Suction Surface

Figure 4 shows the suction surface C_f and C_p distributions. From the C_f distributions the laminar separation bubble onset and reattachment locations, presented in Tab. 4, are obtained. Compared to the DNS the Smagorinsky SGS model is seen to predict the onset of separation much too early, leading to an overly large separation bubble. The WALE and σ SGS models do significantly better here, and this



(a) Suction surface



(b) Pressure surface

FIGURE 3: ISO-SURFACES OF POSITIVE Q-CRITERION COLOURED BY STREAMWISE VORTICITY FOR CASE 1-L-N.

is reflected in the C_p distributions in Fig. 4b. There is however still a slight over-prediction in the bubble length compared to the DNS.

The disagreement between the SGS models arises from the different SGS viscosities they return. Figure 5 shows that the Smagorinsky model incorrectly returns a high SGS viscosity on the edge of the laminar boundary layer upstream of transition. In contrast, since it is pure shear here the WALE (not shown) and σ models predict a very low level of SGS viscosity.

One may hypothesise that the high SGS viscosity from the Smagorinsky model is damping the development of instabilities in the laminar boundary layer, leading to early separation. However, from Fig. 6 it is apparent that, upstream of transition, the suction surface RMS velocities in all three LES cases agree quite well. It is only after the onset of the separation bubble that the Smagorinsky velocity fluctuations begin to deviate significantly from the DNS. Instead it appears, from Fig. 7, that the high eddy viscosity in the laminar boundary layer is causing the boundary layer to grow too fast. The thicker suction surface boundary layer in the Smagorinsky

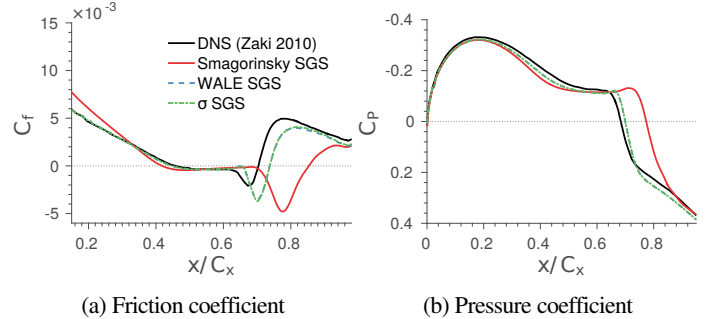


FIGURE 4: SPANWISE AVERAGED C_p AND C_f DISTRIBUTIONS ON SUCTION SURFACE.

TABLE 4: SEPARATION BUBBLE ONSET AND REATTACHMENT LOCATIONS.

	Onset		Reattachment	
	x/C_x	Error (% C_x)	x/C_x	Error (% C_x)
DNS [6]	0.447	N/A	0.705	N/A
Smagorinsky	0.418	-2.9	0.853	+14.8
WALE	0.459	+1.2	0.738	+3.3
σ	0.459	+1.2	0.738	+3.3

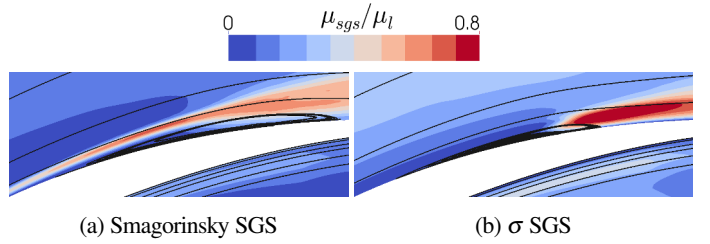


FIGURE 5: CONTOURS OF SPAN-AVERAGED SGS VISCOSITY RATIO AROUND SEPARATION BUBBLE.

simulation, and the adverse pressure gradient, mean that the boundary layer is more susceptible to separation.

The velocity fluctuations from the σ and WALE model simulations mostly agree well with the DNS. The most noticeable difference is that u_{rms} doesn't increase between $0.4 < x/C_x < 0.6$ to the same extent as in the DNS (see Fig. 6a). Zaki et al. [6] note that u_{rms} dominating over v_{rms} and w_{rms} here hints at the presence of Klebanoff streaks [6]. Thus it appears that the magnitude of these Klebanoff modes is under-predicted in the present LES cases, which may help explain the slight over-prediction in bubble length. In the LES computations of Lardeau et al. [10] the opposite is found, with the magnitude of the Klebanoff modes being significantly over-predicted. Future work will investigate the cause of this discrepancy.

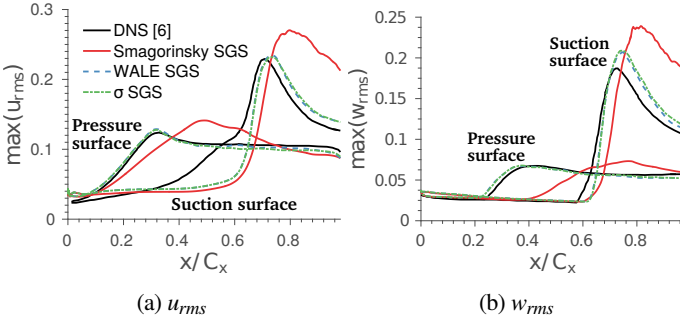


FIGURE 6: WALL NORMAL MAXIMUMS OF STREAMWISE AND SPANWISE VELOCITY FLUCTUATIONS INSIDE THE BOUNDARY LAYER.

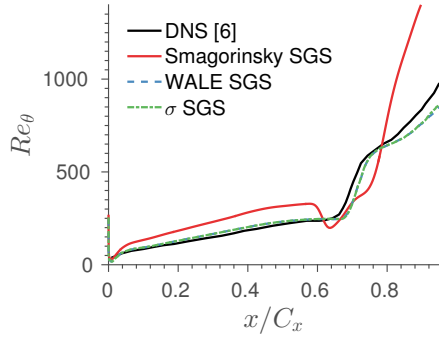


FIGURE 7: SPAN-AVERAGED Re_θ ALONG SUCTION SURFACE.

Pressure Surface

It is obvious from the pressure surface C_f distributions in Fig. 8a that the Smagorinsky model leads to a significant delay in the pressure surface transition location. With the separation induced transition (on the suction surface) the high SGS viscosity from the Smagorinsky model causes excessive boundary layer growth but doesn't damp u_{rms} and w_{rms} . However, examining the velocity fluctuations in Fig. 6, it would appear that u_{rms} and w_{rms} in the pressure surface transition region are being damped by the Smagorinsky model. The high SGS viscosity appears to damp the growth of instabilities associated with natural and bypass transition, leading to delayed transition.

The C_f and C_p distributions in Fig. 8 and the velocity fluctuations in Fig. 6 show that the WALE and σ SGS models agree closely with the pressure surface DNS results.

CASCADE 2: 3D CASE

In the previous section the σ SGS model was shown to predict the transitional processes seen on a compressor blade far better than the Smagorinsky model. For this reason the σ model is used for all the simulations of Cascade 2 discussed in this section.

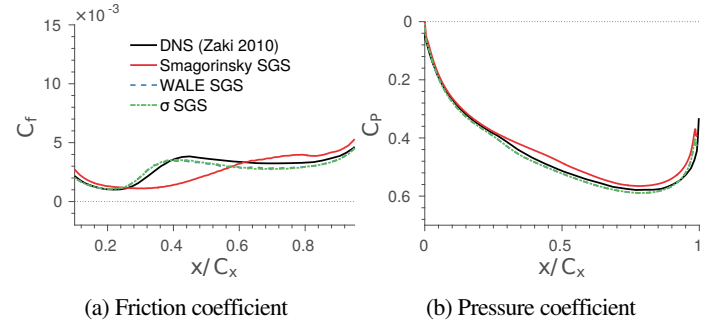


FIGURE 8: PRESSURE SURFACE C_p AND C_f DISTRIBUTIONS.

Validation Against Experiment

Case 2-L-TBL is intended to be representative of the experiment run by Gbadebo et al. [8, 12]. Figure 9 compares the surface limiting streamlines from the time-averaged LES and the experimental oilflow. Qualitatively case 2-L-TBL agrees well with the experiment; a laminar separation bubble is seen on the suction surface in both, the origin of suction surface corner separation is closely predicted, and the corner separation line extends away from the endwall at a similar angle in both. Below the separation line the flow topology also appears to be closely matched.

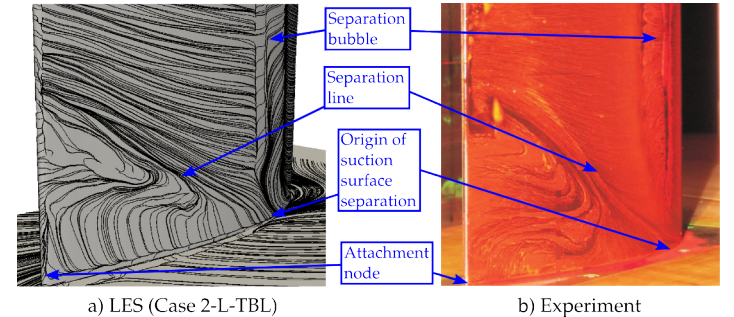


FIGURE 9: LES SURFACE STREAMLINES AND EXPERIMENTAL OILFLOW.

The transitional processes occurring in case 2-L-TBL are visualised using iso-surfaces of Q-criterion in Fig. 10. The processes observed are very similar to those seen on Cascade 1 previously, with separation induced transition on the suction surface and bypass transition on the pressure surface. Also observable is the turbulent endwall boundary layer, and the highly turbulent region in the endwall suction-surface corner.

The C_p distributions for case 2-L-TBL, seen in Fig. 11, generally agree well with the experiment. However, there is some deviation from the experimental C_p distribution close to the trailing edge near the mid-span (Fig. 11b). This isn't due to contamination from the upper inviscid boundary since the spanwise periodic simulation (case

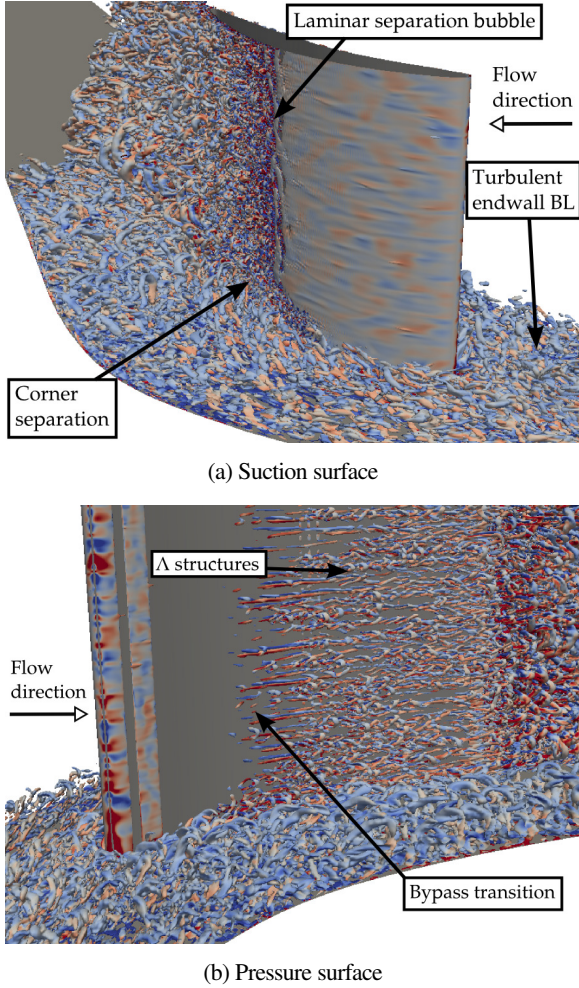


FIGURE 10: CASE 2-L-TBL LES INSTANTANEOUS ISO-SURFACES OF POSITIVE Q-CRITERION COLOURED BY STREAMWISE VORTICITY.

2-L-N) shows the same deviation.

The pitch-wise mass averaged exit angle and loss coefficient are plotted against span in Figures 12a and 12b. The downstream exit angle prediction from case 2-L-TBL is in good agreement with the experiment. The downstream loss prediction also agrees well, with only a slight deficit in the predicted loss between 5% and 25% span. Despite a few small differences between case 2-L-TBL and the experiment, as expected it still gives a much better prediction of the flow compared to a blind RANS computation, as is seen in Figures 11 and 12.

Effect of Endwall Boundary Layer State

The effect of the endwall boundary state (case 2-L-TBL versus case 2-L-LBL) is visualised in Fig. 13. The surface limiting streamlines suggest endwall boundary layer state doesn't significantly affect the flow topology on the blade, especially closer to the

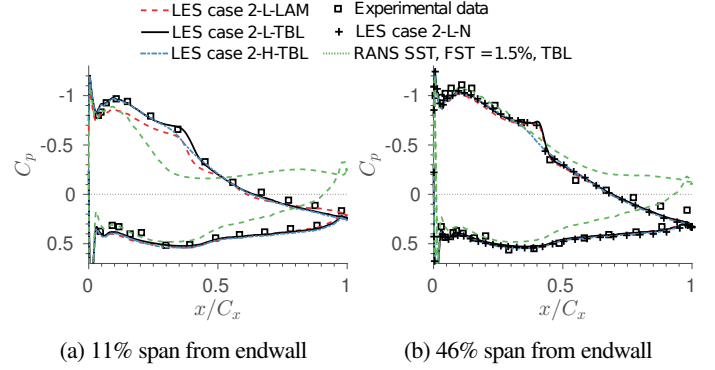


FIGURE 11: C_p DISTRIBUTIONS NEAR ENDWALL AND MID-SPAN.

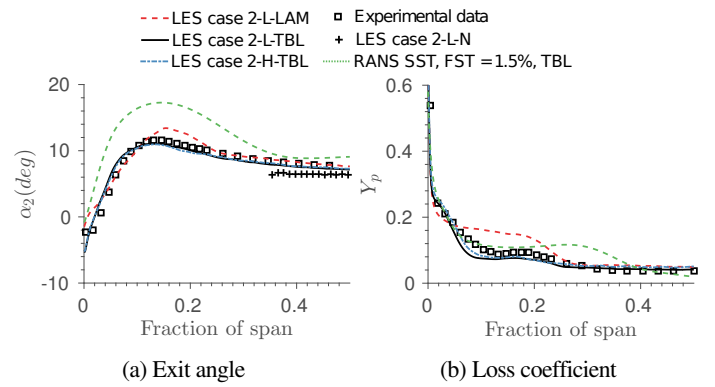


FIGURE 12: PITCHWISE MASS AVERAGED EXIT ANGLE AND LOSS COEFFICIENT VERSUS SPAN.

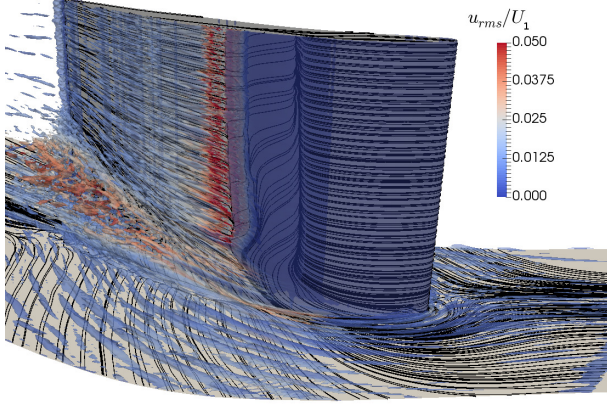
mid-span. The transition location, observable from the peak in u_{rms} (coloured from blue to red), is also not noticeably altered.

The key difference is that the laminar endwall boundary layer can not resist the adverse pressure gradient and so it separates much earlier, observable from the more upstream endwall saddle point in Fig. 13b compared to Fig. 13a. This leads to a much larger pressure leg of the horseshoe vortex which migrates down from the blade above, interacts with the corner separation and results in a large passage vortex, as seen in Fig. 13b.

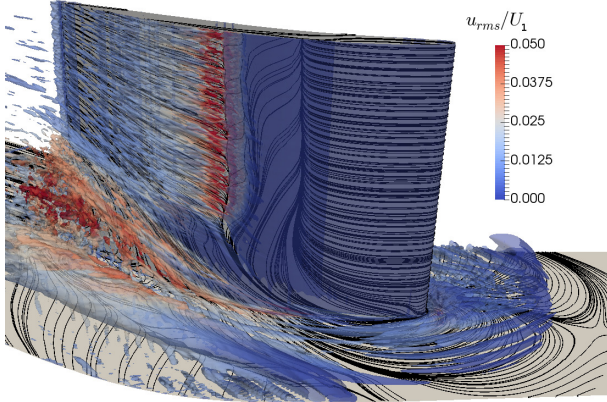
Comparing cases 2-L-TBL and 2-L-LBL in Figures 11a and 12 shows that the larger passage vortex has a significant impact on the pressure distribution, exit flow angle and loss coefficient near the endwall. However, Figures 14 and 15 confirm that the state of the endwall BL has not significantly altered the flow at mid-span.

Effect of Free-Stream Turbulence

Comparing cases 2-L-TBL and 2-H-TBL in Figures 11 and 12 suggests that increasing the FST intensity by an order of magnitude has had little effect on the flow near the endwall. This is surprising, since Goodhand and Miller [4] show that if the transition point moves



(a) Case 2-L-TBL



(b) Case 2-L-LBL

FIGURE 13: TIME-AVERAGED ISO-SURFACES OF VORTICITY MAGNITUDE COLOURED BY u_{rms} .

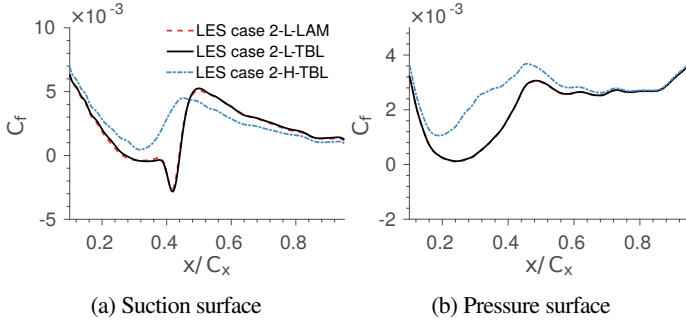


FIGURE 14: FRICTION COEFFICIENT AT MIDSPAN.

upstream the thickened suction surface boundary layer will lead to a larger endwall separation. Figure 14a shows that despite the higher FST intensity changing the suction surface transition mode from separation induced to bypass, the transition location is not altered significantly. Thus it seems that if the transition location is not altered the FST has little influence on the endwall separation.

The velocity fluctuations plotted in Fig. 15 confirm that the

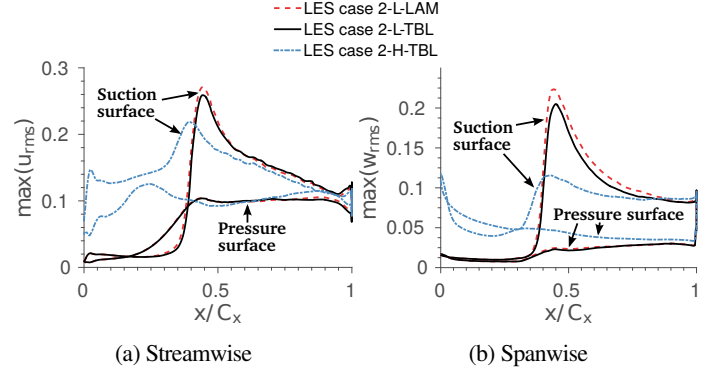


FIGURE 15: WALL NORMAL MAXIMUMS OF STREAMWISE AND SPANWISE VELOCITY FLUCTUATIONS IN THE BLADE PASSAGE AT MIDSPAN.

transition location on the suction surface is similar for both cases. In case 2-H-TBL u_{rms} dominates over v_{rms} and w_{rms} more than in case 2-L-TBL, suggesting the energy carried by Klebanoff modes is higher here. This is consistent with the findings of Zaki et al. [6], where it was found that the energy carried by the Klebanoff modes increases with FST intensity, leading to a faster breakdown of the KH structures and a reduction in the separation bubble length. In case 2-H-TBL the FST intensity is high enough to completely prevent the boundary layer separating.

Figures 14b and 15 show the bypass transition on the pressure surface occurs noticeably earlier with the higher free-stream turbulence. However, the pressure surface - endwall corner effects are relatively small so the pressure surface boundary layer is less important.

Sources of Loss

The previous sections have shown that the state of the suction surface boundary layer and the free-stream turbulence both influence the loss in the passage. To determine the sources of loss and examine the effect of the inflow conditions further the mean flow energy equation is used:

$$\frac{\partial E}{\partial t} + \bar{u}_j \frac{\partial E}{\partial x_j} = \underbrace{\frac{\partial}{\partial x_j} \left(-\bar{u}_j \frac{\bar{p}}{\rho} + 2v\bar{u}_j \bar{s}_{ij} - \bar{u}_i \bar{u}'_j \bar{u}_i \right)}_{\text{Transport}} + \underbrace{-2v\bar{s}_{ij} \bar{s}_{ij} + \bar{u}'_i \bar{u}'_j \bar{s}_{ij}}_{\substack{\text{Viscous} \\ \text{-VD}}} + \underbrace{\bar{u}'_i \bar{u}'_j \bar{s}_{ij}}_{\substack{\text{Turbulent} \\ \text{-TD}}} \quad (6)$$

In Eqn. 6 the viscous and turbulent dissipation terms are the only sink (or source) terms. The viscous dissipation represents the dissipation of mean-flow energy by the velocity gradients, and is always negative (i.e. $VD > 0$). The turbulent dissipation represents the energy transfer from the mean flow into turbulent fluctuations. It is usually negative (i.e. $TD > 0$), meaning energy is being transferred from the mean

flow, however on some occasions it can be positive (i.e. $TD < 0$) implying the presence of turbulent energy backscatter. In cases 2-L-LBL and 2-L-TBL a negative value of TD is observed in the separation bubble region. This is in agreement with the work of Germano et al. [20]. They found that during the early non-linear stages of transition, energy is transferred from smaller to larger scales, even in the mean. However, in the present investigation no negative TD values are observed in the endwall separation region, suggesting there is no backscatter here (at least within the scales resolved). This implies that adding a non-linear term to the SGS model to account for backscatter may not be necessary in the endwall region.

Denton and Pullan [26], and Zlatinov et al. [27], use the entropy generation rate to examine the loss sources in a turbine cascade. In a similar way the TD and VD terms will be used here to examine the loss sources. The flow here is isentropic therefore the thermal dissipation does not need to be considered. To differentiate the loss sources caused by the endwall flow the domain is split into two sections (shown in Fig. 17); a lower section (0-35% span) where endwall effects mean the flow is highly three-dimensional, and an upper section (35-50% span) where the flow is largely two dimensional. The VD and TD terms are then area averaged (in the pitchwise and spanwise directions), and plotted against axial distance. In the upper section (Fig. 16a) there are three distinct peaks which identify the high loss generation areas here:

Leading edge ($x/C_x \approx 0.0$)

VD is high here due to the very high strain rates near the leading edge. This sink is insensitive to the inflow conditions.

2D separation bubble ($x/C_x \approx 0.4$)

TD is high here due to the high level of turbulence generated in the free shear layer at the edge of the 2D separation bubble, which was observed in Fig. 15. Since in case 2-H-TBL the separation bubble is suppressed the peak in TD here is lower than for case 2-L-TBL. However, the higher FST intensity in the passage and the earlier pressure surface transition mean that the TD increases earlier in case 2-H-TBL. The state of the endwall BL has little effect here.

Trailing edge shear layer ($x/C_x \approx 1.1$)

TD is high here due to the turbulence generated in the free shear layer at the edges of trailing edge wake. The inflow conditions appear to have little effect here.

In the lower section close to the endwall (Fig. 16b) the three distinct peaks are still present. However, now there is also an area of high turbulent dissipation downstream ($x/C_x > 0.5$) caused by the three dimensional flow near the endwall. The FST intensity has little influence on the loss in this region, further supporting the conclusion that the 3D endwall flow is insensitive to the FST intensity.

The laminar endwall boundary layer case (2-L-LBL) shows significantly higher turbulent dissipation in the 3D separation region near the endwall ($x/C_x > 0.5$ in Fig. 16b). Figure 17 presents contours of turbulent dissipation at three locations ($x/C_x = 0.41, 0.7, 1.1$), for the turbulent and laminar endwall BL cases:

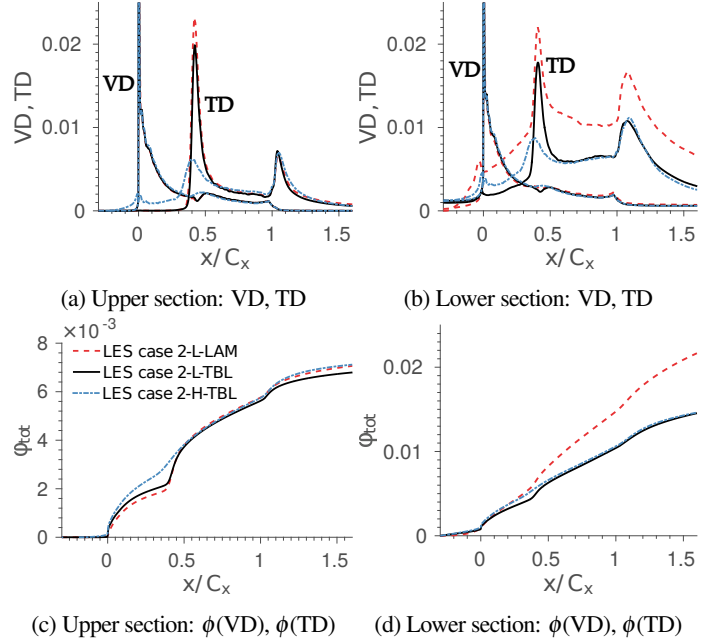


FIGURE 16: AREA AVERAGED VISCOUS AND TURBULENT DISSIPATION IN UPPER AND LOWER SPAN, AND CUMULATIVE INTEGRAL OF BOTH QUANTITIES.

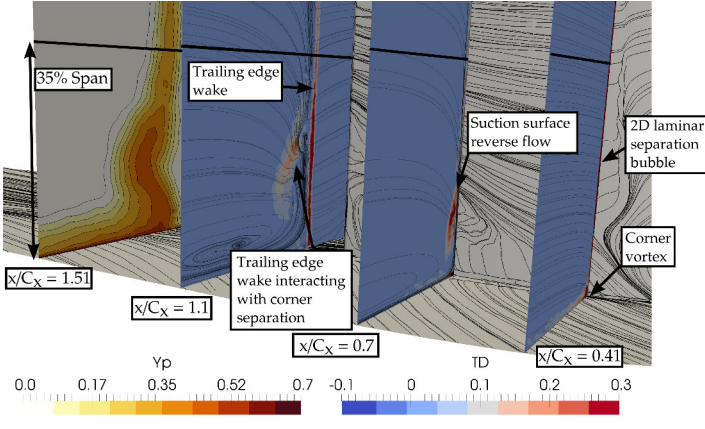
Figure 17a: Case 2-L-TBL The TD is high in the 3D separation region where there is reverse flow on the suction surface (seen at $x/C_x = 0.7$), and this 3D separation region persists downstream at $x/C_x = 1.1$.

Figure 17b: Case 2-L-LBL There is also high TD in the shear layer between the passage vortex and the free-stream, and the TD is especially high where the passage vortex interacts with the corner separation close to the suction surface. This high TD causes significantly higher loss, which is observable when comparing the pressure loss coefficient (Y_p) contours downstream of the blade in Figures 17a and 17b.

The overall effect of the VD and TD on the loss can be seen by plotting the cumulative integral of the sum of these terms with respect to the axial direction:

$$\phi_{tot}(X) = \int_{x=-0.45C_x}^{x=X} (TD(x) + VD(x)) dx \quad (7)$$

where $\phi_{tot}(X)$ is the total area averaged dissipation (VD + TD) so far (i.e. between $-0.45C_x < x < X$). This is plotted against x in Figures 16c and 16d. Near the mid-span (Fig. 16c), the high FST intensity in case 2-H-TBL causes a higher ϕ_{tot} early on due to the early pressure surface transition and higher FST intensity in the passage. However, ϕ_{tot} in the other two cases rapidly increases to rejoin case 2-H-TBL due to the high TD in the separation bubble at $x/C_x \approx 0.4$. By the outflow plane at $x/C_x = 1.52$ the total dissipation in the upper section is very similar for all three cases, with case



(a) Case 2-L-TBL

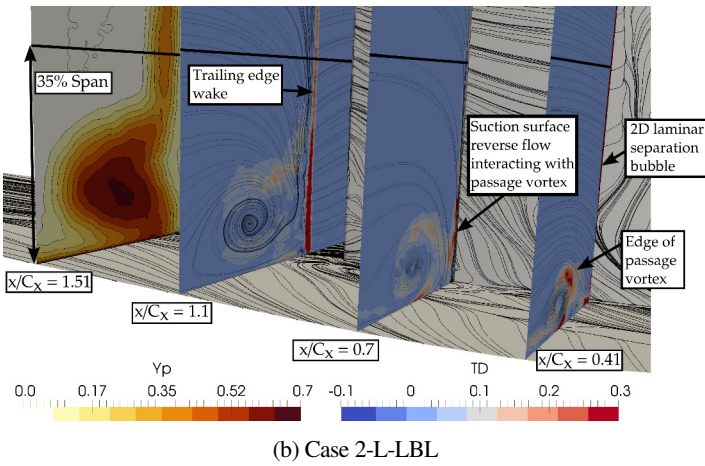


FIGURE 17: CONTOURS OF TURBULENT DISSIPATION AND LOSS COEFFICIENT NEAR ENDWALL.

2-L-TBL having a slightly lower total. These findings correlated well with the loss coefficient plot in Fig. 12b where the loss at mid-span is slightly lower for case 2-L-TBL.

Near the endwall (Fig. 16d) where 3D flow effects are significant the FST has little effect, with the ϕ_{tot} lines for both FST cases following closely. Conversely, ϕ_{tot} increases more rapidly in the LBL case downstream of the separation bubble ($x/C_x > 0.5$) due to the effects of the passage vortex discussed previously. Again, these findings correlate well with the loss coefficient distribution in Fig. 12b. Near the endwall the loss in the high and low FST intensity cases are very similar, whereas the loss in the LBL case is much higher here.

Turbulence Characteristics

Gbadebo [8] used a hotwire probe to measure the RMS of the mean velocity, U'_{RMS} . This gives an indication of the local turbulence intensity in the endwall region. Figure 18 shows that at the trailing edge the distribution of U'_{RMS} in LES case 2-L-TBL is in good

agreement with the experiment of Gbadebo [8]. The LES is slightly under-predicting the maximum value of U'_{RMS} , seen downstream of the corner separation. This is partly expected since the LES isn't resolving all the scales of turbulence. Also, the King/Jørgensen model used by Gbadebo [8] to calibrate the hotwire probe can be inaccurate when the turbulence has high intensity or anisotropy [28].

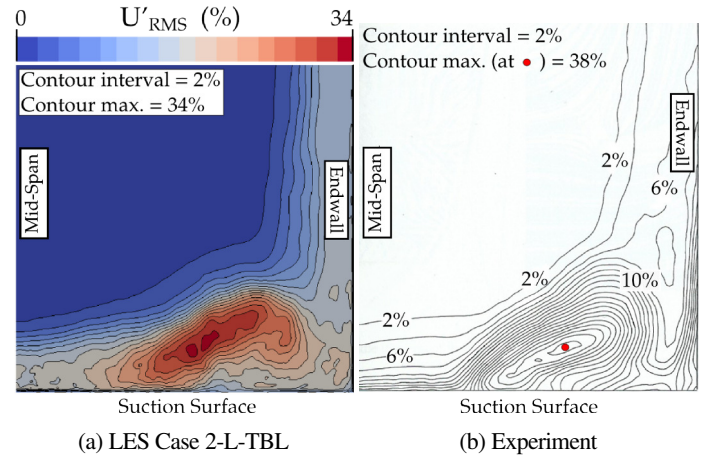


FIGURE 18: CONTOURS OF RMS OF MEAN VELOCITY AT TRAILING EDGE, LES VS. HOTWIRE MEASUREMENTS.

The high U'_{RMS} in the endwall region suggests a possible contribution of endwall separation to broadband noise. Moreover, the significant difference in turbulence intensity between the endwall separation and the FST may help explain why the endwall separation has been found to be relatively insensitive to the FST intensity.

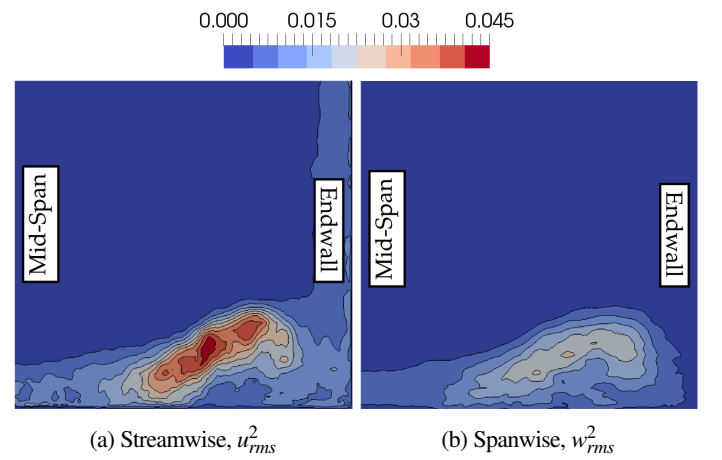


FIGURE 19: CONTOURS OF VELOCITY FLUCTUATIONS AT TRAILING EDGE, FOR LES CASE 2-L-TBL.

Examining the separate velocity components shows that the turbulence is anisotropic in the corner separation region. The streamwise fluctuations (Fig. 19a) dominate over the pitch-wise (not shown) and spanwise (Fig. 19b) fluctuations. This has consequences for RANS modelling of such flows, since many RANS models do not correctly account for anisotropy of turbulence.

CONCLUSIONS

The following conclusions are drawn from this study:

1. The Smagorinsky sub-grid scale model is unsuitable for the transitional compressor flows studied. It causes excessive thickening of the suction surface boundary layer, leading to premature separation, and an over-prediction of the bubble length. On the pressure surface it significantly delays the bypass transition. In comparison, the ability of the σ and WALE models to limit the SGS viscosity in the laminar boundary layer means they are more suitable to such flows. These purely local SGS models appear to be able to compete with the dynamic SGS models used by Lardeau et al. [10] for the same case. The ability to use local SGS models will simplify the application of LES to more complex compressor geometries.
2. The state of the endwall boundary layer is critical. A laminar endwall boundary layer cannot withstand the adverse pressure gradient near the leading edge and so separates earlier. The larger passage vortex leads to under-turning of the flow and increased loss. In many blade cascade experiments the endwall boundary layers are partly relaminarised by an upstream contraction. This highlights the need for the endwall boundary layer velocity and stress profiles to be accurately recorded in cascade experiments.
3. Increasing the FST intensity caused the suction surface transition mode to change from separation induced to bypass transition. However, this had little effect on the corner separation since the transition location, and therefore the boundary layer thickness, was unaffected. Additionally, the FST was not found to directly influence the corner separation, perhaps due to the much higher turbulence intensity observed in the corner separation region.
4. Near the mid-span the viscous dissipation near the leading edge and turbulent dissipation at the 2D separation bubble are the main loss sources. A high FST intensity suppresses the separation bubble, but causes higher loss overall due to the earlier pressure surface transition and higher turbulent dissipation in the free-stream. In the 3D flow region near the endwall the turbulent dissipation dominates. The FST intensity has little effect here. The state of the endwall boundary layer and the size of the passage vortex it results in are more important.

ACKNOWLEDGMENT

This work was supported by the EPSRC through an iCASE award sponsored by Rolls-Royce plc. Rolls-Royce plc are gratefully

acknowledged for allowing the use and modification of their CFD solver *Hydra*. The work used the ARCHER UK National Supercomputing Service (<http://www.archer.ac.uk>) under EPSRC grant EP/L000261/1, and thanks go to both for their support. Finally, the authors would like to thank Dr. Naqavi, Dr. Watson, and Mr. Cui for their invaluable inputs, Dr. Zaki for providing the geometry for cascade 1, and Dr. Lardeau for providing the inflow turbulence code.

NOMENCLATURE

x,y,z	Axial, pitchwise, spanwise co-ordinates
Re	Reynolds number
T_i	Free-stream turbulence intensity
i	Incidence angle
α_2	Exit flow angle
h	Blade height/span
S	Blade pitch
t	Blade thickness
C	Blade chord
C_x	Blade axial chord
C_p	Static pressure coefficient, $(p - p_1)/(\frac{1}{2}\rho U_1^2)$
Y_p	Total pressure loss coefficient, $(p_{01} - p_0)/(\frac{1}{2}\rho U_1^2)$
C_f	Skin friction coefficient, $\mu_l(\tau_w)/(\frac{1}{2}\rho U_1^2)$
u_τ	Friction velocity, $\sqrt{\tau_w/\rho}$
U_1	Inflow bulk velocity
d	Wall distance
k	Turbulent kinetic energy
ε	Turbulent dissipation
L	Integral length scale of turbulence
L_e	Dissipation length scale of turbulence
T^*	Flow through time
δ_0	Boundary layer thickness based on $0.99U_1$
δ^*	Boundary layer displacement thickness
θ	Boundary layer momentum thickness
H	Boundary layer shape factor, δ^*/θ
μ_{sgs}	Sub-grid scale viscosity
Δ^+	Non-dimensional grid spacing at wall, $\Delta \sqrt{\tau_w/\rho}/v$
Δ_{vol}	Cell volume filter, $\sqrt[3]{\Delta x \Delta y \Delta z}$
Δ_{SGS}	Sub-Grid scale model filter
Q	Q-criterion, $\frac{1}{2}(\Omega ^2 - \mathcal{S} ^2)$
S/Ω	Magnitude of strain rate/vorticity tensor, $\sqrt{2S_{ij}S_{ij}}, \sqrt{2\Omega_{ij}\Omega_{ij}}$
S_{ij}/Ω_{ij}	Strain rate/Vorticity tensors
μ_l/μ_t	Laminar/Turbulent viscosity
$\sigma_{1/2/3}$	Singular values of the resolved velocity gradient tensor
U'_{RMS}	RMS mean velocity, $\sqrt{1/2(u_{rms}^2 + v_{rms}^2 + w_{rms}^2)}$
$u_{rms}, v_{rms}, w_{rms}$	Streamwise, wall-normal and spanwise RMS velocities

Subscripts

- FS Free-stream quantity
- 1 Inflow quantity
- 2 Exit quantity

Abbreviations

- SGS** Sub-Grid Scale
- MTS** Mixed Time-Scale
- FST** Free-Stream Turbulence
- CDA** Controlled Diffusion Aerofoil
- TD** Turbulent Dissipation
- VD** Viscous Dissipation
- RMS** Root Mean Square
- KH** Kelvin-Helmholtz
- TS** Tollmien-Schlichting
- LBL** Laminar Boundary Layer
- TBL** Turbulent Boundary Layer

REFERENCES

- [1] Dong, Y. et al., 1987. “Three-Dimensional Flows and Loss Reduction in Axial Compressors”. *J. Turbomach.*, **109**(3), jul, p. 354.
- [2] Friedrichs, J. et al., 2001. “Effect of Stator Design on Stator Boundary Layer Flow in a Highly Loaded Single-Stage Axial-Flow Low-Speed Compressor”. *J. Turbomach.*, **123**(3), jul, p. 483.
- [3] Lei, V. M. et al., 2008. “A Criterion for Axial Compressor Hub-Corner Stall”. *J. Turbomach.*, **130**(3).
- [4] Goodhand, M. N., and Miller, R. J., 2012. “The Impact of Real Geometries on Three-Dimensional Separations in Compressors”. *J. Turbomach.*, **134**(2), p. 021007.
- [5] Gbadebo, S. A. et al., 2004. “Influence of Surface Roughness on Three-Dimensional Separation in Axial Compressors”. *J. Turbomach.*, **126**(4), oct, p. 455.
- [6] Zaki, T. a. et al., 2010. “Direct numerical simulations of transition in a compressor cascade: the influence of free-stream turbulence”. *J. Fluid Mech.*, **665**, oct, pp. 57–98.
- [7] Steinert, W., and Starken, H., 1996. “Off-Design Transition and Separation Behavior of a CDA Cascade”. *J. Turbomach.*, **118**(2), apr, p. 204.
- [8] Gbadebo, S. A., 2003. “Three-Dimensional Separations in Compressors”. PhD thesis, University of Cambridge.
- [9] Denton, J. D., 1993. “The 1993 IGTI Scholar Lecture: Loss Mechanisms in Turbomachines”. *J. Turbomach.*, **115**(4), oct, p. 621.
- [10] Lardeau, S. et al., 2011. “Large Eddy Simulation of Transitional Separated Flow over a Flat Plate and a Compressor Blade”. *Flow, Turbul. Combust.*, **88**(1-2), jul, pp. 19–44.
- [11] Hilgenfeld, L., and Pfitzner, M., 2004. “Unsteady Boundary Layer Development Due to Wake Passing Effects on a Highly Loaded Linear Compressor Cascade”. *J. Turbomach.*, **126**(4), p. 493.
- [12] Gbadebo, S. A. et al., 2005. “Three-Dimensional Separations in Axial Compressors”. *J. Turbomach.*, **127**(2), apr, pp. 331–339.
- [13] Piomelli, U., and Chasnow, J. R., 1996. “Large-eddy simulations: theory and applications”. In *Transit. Turbul. Model.*, D. Henningson, et al., eds. Kluwer Academic Publishers, Dordrecht, pp. 269–336.
- [14] Spalart, P. R., and Rumsey, C. L., 2007. “Effective Inflow Conditions for Turbulence Models in Aerodynamic Calculations”. *AIAA J.*, pp. 1–14.
- [15] Crumpton, P. et al., 1997. “An unstructured algorithm for high Reynolds number flows on highly stretched grids”. *Tenth Int. Conf. Numer. methods laminar Turbul. flow*, pp. 1–13.
- [16] Rogers, S. E. et al., 1991. “Steady and unsteady solutions of the incompressible Navier-Stokes equations”. *AIAA J.*, **29**(4), apr, pp. 603–610.
- [17] Cui, J. et al., 2015. “Numerical Investigation of Contrasting Flow Physics in Different Zones of a High-Lift Low-Pressure Turbine Blade”. *J. Turbomach.*, **138**(1), oct, p. 011003.
- [18] Cui, J. et al., 2015. “Numerical investigation of secondary flows in a high-lift low pressure turbine”. In 8th Int. Symp. Turbul. Heat Mass Transf.
- [19] Smagorinsky, J., 1963. “General Circulation Experiments with the Primitive Equations”. *Mon. Weather Rev.*, **91**(3), mar, pp. 99–164.
- [20] Germano, M. et al., 1991. “A dynamic subgrid-scale eddy viscosity model”. *Phys. Fluids A Fluid Dyn.*, **3**(7), jul, p. 1760.
- [21] Nicoud, F., and Ducros, F., 1999. “Subgrid-Scale Stress Modelling Based on the Square of the Velocity Gradient Tensor”. *Flow, Turbul. Combust.*, **62**(3), pp. 183–200.
- [22] Nicoud, F. et al., 2011. “Using singular values to build a subgrid-scale model for large eddy simulations”. *Phys. Fluids*, **23**(8), pp. 1–35.
- [23] Lund, T. S. et al., 1998. “Generation of Turbulent Inflow Data for Spatially-Developing Boundary Layer Simulations”. *J. Comput. Phys.*, **140**(2), mar, pp. 233–258.
- [24] Spalart, P. R., 1988. “Direct simulation of a turbulent boundary layer up to $R\theta = 1410$ ”. *J. Fluid Mech.*, **187**, pp. 61–98.
- [25] Rogallo, R. S., 1981. Numerical experiments in homogeneous turbulence. Tech. rep., NASA Ames Research Center, Moffett Field, CA. Report No. NASA-TM- 81315.
- [26] Denton, J., and Pullan, G., 2012. “A numerical investigation into the sources of endwall loss in axial flow turbines”. In Proc. ASME Turbo Expo, pp. 1–14.
- [27] Zlatinov, M. B. et al., 2012. “Turbine Hub and Shroud Sealing Flow Loss Mechanisms”. *J. Turbomach.*, **134**(6), nov, p. 061027.
- [28] Dijk, A. V., and Nieuwstadt, F. T. M., 2004. “The calibration of (multi-)hot-wire probes. 2. Velocity-calibration”. *Exp. Fluids*, **36**, pp. 550–564.